# Measurement of the Triple Differential Photon Plus Heavy-Flavor Jet Cross Section in $p\bar{p}$ Collisions at $\sqrt{s} = 1.96$ TeV in D0

The DØ Collaboration
*URL http://www-d0.fnal.gov*
(Dated: July 25, 2008)

Measurements of triple differential cross sections $\mathrm{d}^3\sigma/(\mathrm{d}p_T^\gamma \mathrm{d}y^\gamma \mathrm{d}y^{\mathrm{jet}})$ for the production of $\gamma + b$-jet+X and $\gamma + c$-jet+X events are presented for photon transverse momenta in the range 30–150 GeV with photon rapidities of $|y^\gamma| < 1.0$ and jet rapidities of $|y^{\mathrm{jet}}| < 0.8$. The results are based on a data sample of 1 fb$^{-1}$ of integrated luminosity accumulated between September 2002 and February 2006 in $p\bar{p}$ collisions at $\sqrt{s} = 1.96$ TeV and recorded with the D0 detector at the Fermilab Tevatron Collider. The results are compared with next-to-leading order QCD predictions using CTEQ6.6M parton distribution functions.

*Preliminary Results for Summer 2008 Conferences*

# I. INTRODUCTION.

Due to the electromagnetic nature of photon-quark interactions, the photons produced in the final state of fundamental $2 \to 2$ QCD interactions provide a valuable source of information about parton dynamics in the initial state [1–9]. In high energy $p\bar{p}$ collisions a dominant source for production of photons with a high transverse momentum $p_T$ are direct photons. Direct photons produced in association with heavy ($c$ or $b$) quarks provide a possibility to better understand the proton/antiproton properties and, in particular, to measure the momentum distributions of its constituent heavy quarks [9, 10].

The two main sources of the associated photon ($\gamma$) and heavy flavor quark ($Q$) production are the "Compton"-like scattering

$$Q + g \to Q + \gamma \tag{1}$$

with $Q = c, b$ and the "annihilation" subprocess

$$q + \bar{q} \to g + \gamma \tag{2}$$

where the final state gluon splits into a heavy quark pair $g \to Q\bar{Q}$. The first process is dominant in a large kinematic range, while the second one becomes dominant at $p_T^\gamma > 80$–100 GeV. Figure 1 shows the fractional contributions of the $Qg \to Q\gamma$ subprocesses to the total cross section of associated production of a direct photon and a heavy flavor quark in the two kinematic regions described below. The fractions are obtained using signal processes (1) and (2) simulated with the Monte Carlo (MC) event generator PYTHIA [13] with the CTEQ6L PDF set [14].
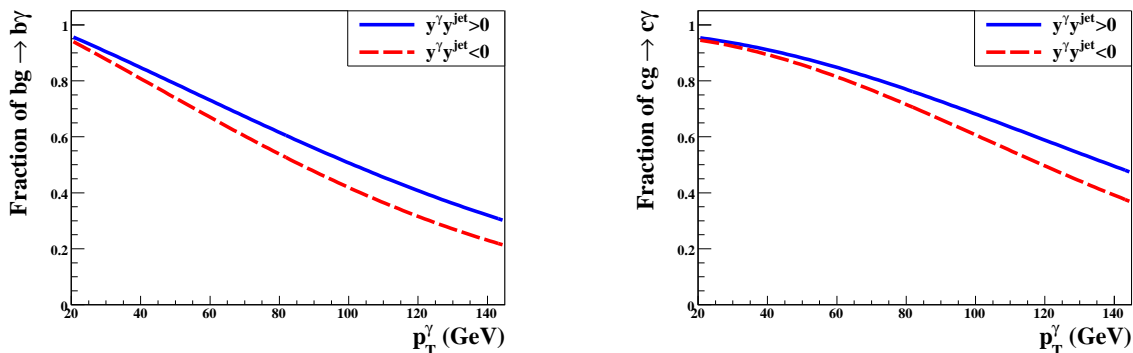


FIG. 1: Fractional contribution of the $Qg \to Q\gamma$ subprocess to the associated production of direct photon and heavy-flavor jet in regions 1 and 2. Left: for events with at least one $b$-quark. Right: for events with at least one $c$-quark. The fractions are calculated using PYTHIA 6.3, CTEQ6L, and imposing the following cuts on the photon and leading quark: $|y^\gamma| < 1$, $|y^Q| < 0.8$, $p_T^Q > 15$ GeV.

The production cross section for process (1) is obviously sensitive to the $b$ and $c$ quark and gluon densities inside the colliding hadrons and may give us an opportunity for tuning the parameters of those PDFs which still have noticeable uncertainties [15, 16]. Those uncertainties, on the theory side, come from a scheme dependence in the treatment of the heavy flavor quarks and the choice of specific parameters (like heavy quark thresholds) in some schemes [15–17]. On the experimental side several relevant measurements exist [18–23], but they cannot impose stringent constraints on the kinematic regions accessible at the Tevatron or the LHC for many interesting physics processes (for example, single top or Higgs boson production in various models [24–27]).

Additional uncertainties are also caused by the heavy quark fragmentation process and by the gluon splitting $g \to Q\bar{Q}$. These contain non-perturbative corrections in theory and about 15–25 % in uncertainties found from averaging over the LEP/SLD data [28].

This note presents the first measurements of $\gamma$ + bottom and $\gamma$ + charm triple differential cross sections $\mathrm{d}^3\sigma/(\mathrm{d}p_T^\gamma \mathrm{d}y^\gamma \mathrm{d}y^{\mathrm{jet}})$ in $p\bar{p}$ collisions at $\sqrt{s} =$1.96 TeV. The data sample corresponds to $1.022 \pm 0.061$ fb$^{-1}$ recorded using the D0 detector at the Fermi National Accelerator Laboratory. In this measurement the photon and leading jet are located in the central rapidity region with $|y^\gamma| < 1.0$ and $|y^{\mathrm{jet}}| < 0.8$ with the photon transverse momentum $p_T^\gamma$ covering a range from 30 to 150 GeV. The leading jet is required to have $p_T^{\mathrm{jet}} > 15$ GeV.

By analogy to a previous D0 "$\gamma$+jet" analysis [29], the cross sections are measured in the following two kinematic regions:

- region 1: $(0.0 < y^\gamma < 1.0$ and $0.0 < y^{\text{jet}} < 0.8)$     or $(-1.0 < y^\gamma < 0.0$ and $-0.8 < y^{\text{jet}} < 0.0)$;

- region 2: $(0.0 < y^\gamma < 1.0$ and $-0.8 < y^{\text{jet}} < 0.0)$    or $(-1.0 < y^\gamma < 0.0$ and $0.0 < y^{\text{jet}} < 0.8)$.

As we see, region 1 is characterized by a positive product of photon and jet rapidities $y^\gamma y^{\text{jet}} > 0$, while region 2 corresponds to a negative product $y^\gamma y^{\text{jet}} < 0$. These two rapidity combinations allow one to better differentiate regions of the parton momentum-fraction space for the two initial interacting partons, $x_{1,2}$. For all interaction energy scales, region 1 covers different $x_1$ and $x_2$ intervals, while region 2 correspond to events with similar $x_1$ and $x_2$ intervals. For example, at $p_T^\gamma = 35$ GeV region 1 covers the intervals $0.01 \lesssim x_1 \lesssim 0.03$ and $0.03 \lesssim x_2 \lesssim 0.09$, while $x_1$ and $x_2$ for region 2 correspond to the same interval of $0.02 \lesssim x_{1,2} \lesssim 0.06$. Here $x_1$ and $x_2$ are calculated using the leading-order expression $x_{1,2} = p_T^\gamma/\sqrt{s} \cdot [\exp(\pm y^\gamma) + \exp(\pm y^{\text{jet}})]$ [3].

A measurement of the triple differential cross section at the Fermilab Tevatron should allow us to get information about $b$, $c$, and gluon PDFs in the $x$ range of $0.01 < x < 0.3$ with $0.9 \times 10^3 < (p_T^\gamma)^2 < 2 \times 10^4$ GeV$^2$.

## II. EVENT AND OBJECT SELECTION.

### A. Event Selection And Detector Description.

Events are selected to have a primary collision vertex within 50 cm from the center of the detector along the beam axis and to be reconstructed with three or more tracks. These criteria are 99.8 % efficient for data events after requiring the leading jet in the event to be *taggable* (see section II C). In order to reject background events caused by cosmics and $W \to e\nu$ decays, we require the missing transverse energy in the event to be less than $0.7 p_T^\gamma$.

This analysis largely utilizes the central-tracking system, consisting of a silicon microstrip tracker (SMT) and a central fiber tracker (CFT) with coverage in pseudorapidity of $|\eta| < 3$ and $|\eta| < 2.5$, respectively. The SMT provides high resolution stereo position measurements with 792,576 channels, which is crucial for correctly identifying displaced tracks and vertices of the heavy flavor jet decays. The tracking system is located within a 2 T superconducting solenoidal magnet. It is followed by the central preshower detector (CPS, $|\eta| < 1.2$) with three concentric cylindrical layers of scintillator strips. The D0 calorimeter is a liquid argon sampling calorimeter enclosed in three hermetic cryostats and covers an $|\eta|$ range up to 4.2. It is used to reconstruct both the photon candidate and jets with ∼48,000 finely segmented channels. The calorimeter is separated into electromagnetic (EM) and hadronic layers with cell sizes of $\Delta\eta \times \Delta\phi = 0.1 \times 0.1$ and $0.05 \times 0.05$ in the shower max layer (EM3). High energy towers are used to create clusters of energy in the EM calorimeter in a cone of radius $R \equiv 0.4$, where $R$ is the distance in the $\eta$-$\phi$ space, $R = \sqrt{\Delta\eta^2 + \Delta\phi^2}$. Once an EM energy cluster is formed, the final energy used is taken from a smaller cone of $R \equiv 0.2$.

### B. Trigger And Photon Candidate Selection.

The triggers used in this analysis identify clusters of large electromagnetic energy in events and are based on the photon $p_T$ and loosely on the photon shower shape. These triggers are ∼ 97 % efficient at $p_T^\gamma \simeq 30$ GeV and are more than 99 % efficient at $p_T^\gamma > 35$ GeV. In each event the highest $p_T$ photon is selected and is required to have more than 96 % of its total energy in the EM layers of the calorimeter. The photon candidates must also be well isolated within the calorimeter. We require that the total amount of excess hadronic and EM energy surrounding the EM cluster inside a cone of radius $R \equiv 0.4$ to be less than 7 % of the EM cluster's total energy. We also require the energy-weighted shower width in the EM3 layer to be consistent with that of an electromagnetic shower.

The probability of any track to be spatially matched to the EM cluster in the event is required to be less than 0.1 %. The primary collision vertex is further constrained using a combined calorimeter and preshower layer "pointing." This requirement utilizes the layer positions of the energy cluster to extrapolate to the region along the beampipe from where the photon candidate most likely originated. With a preshower confirmation of the EM cluster position, the primary vertex $z$ position must lie within 10 cm of the extrapolated position.

In order to further reject particles such as $\pi^0$, $\eta$ mesons and others that can mimic the photon candidate signature, an artificial neural network (ANN) was developed to provide additional suppression of these backgrounds [29]. The input variables used in this neural network include the number of cells in the EM cluster from the first calorimeter EM layer, the fraction of the photon candidate energy deposited in the first EM layer, and the sum of track energies between two cones of radius $R \equiv 0.05$ and $R \equiv 0.4$ centered about the direction of the EM cluster. The calculated ANN output for the candidate photon is required to be greater than 0.7.

The photon efficiencies for the photon selection criteria described above are corrected for data/MC efficiency differences using $Z \to ee$ and $Z\gamma$ events [30]. The total efficiency versus $p_T^\gamma$ is shown in Fig. 2.
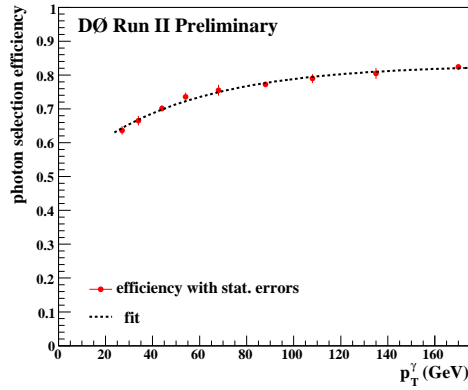
FIG. 2: The total photon selection efficiency to pass the photon criteria of section II B as a function of $p_T^\gamma$.

The total photon selection systematic uncertainty varies within 4.9–5.2 % and is caused mainly by the anti-track match cut (3 %), the data/simulation correction from $Z \to ee$ events (1.5–2 %), the ANN cut (2.4 %), the photon vertex pointing requirement (2 %), and the uncertainty on the parameterized photon selection efficiency ($\sim 1$ %).

### C.   Heavy Flavor Jet Candidate Selection.

Events containing at least one hadronic jet are selected. Jets are reconstructed using the D0 RunII jet-finding algorithm [11] with a cone of radius $R \equiv 0.5$. The leading $p_T$ jet is required to have $p_T > 15$ GeV and $|y| < 0.8$. Particle level $c$ and $b$ jets[1] from $\gamma$+jet MC events were matched to the reconstructed ones to estimate the reconstruction efficiency of the jets as well as the $p_T$ ordering effects of the jets where a non-leading jet would be reconstructed as the highest $p_T$ jet in the event. The efficiency for a jet to be reconstructed and to pass the jet identification criteria is 93 % (94.5 %) for light (b) jets at $p_T^\gamma = 30$ GeV and increases to $\sim 98$ % at $p_T^\gamma = 150$ GeV, independent of the jet flavor. The impact from jet energy scale (JES) uncertainties on the $p_T$-threshold requirement was studied by varying the jet $p_T$ within the uncertainties from the JES corrections, the energy resolution and an additional uncertainty caused by the different energy response of light and $b$-jets. The latter uncertainty is taken as the actual difference in response between light and $b$ jets as predicted by the simulation and accounts for about 17 % uncertainty for $b$-jets at $p_T^{\text{jet}} = 15$ GeV and decreases to $\sim 9$ % at $p_T^{\text{jet}} = 150$ GeV. All three uncertainties combined lead to a total uncertainty between $\sim 8$ % and 2 % on the selected mixture of jet flavors in data. The leading jet is also required to have at least one associated track with $p_T > 1.0$ GeV (to be used as the seed track), at least one other associated track with $p_T > 0.5$ GeV, and track proximity requirements to the reconstructed jet. The track needs to have at least one SMT hit. These criteria (*taggability*) are applied to ensure that the jet will contain enough information to be properly identified as a heavy flavor jet candidate.

In order to suppress jets not originating from either a $c$ or $b$ meson, a neural network is applied that exploits the longer lifetimes of these particles in comparison to their lighter counterparts [12]. The neural network ($b$-NN) combines several characteristic input quantities into a continuous output value between zero and one. The input variables are the number of reconstructed secondary vertices in the jet, the mass of the secondary vertex, the number of tracks used to reconstruct the secondary vertex, the decay length significance of the secondary vertex, a weighted combination of the tracks' impact parameter significances and the probability that a jet originates from the primary vertex, which is referred to as the JLIP probability. The neural net output tends towards values close to one for $b$ jets and towards zero for non-$b$ jets. In this analysis, the leading jet is required to have a neural net value greater than 0.85. In addition it is required that the *JLIP reduced probability* could be calculated. The JLIP tagger calculates the probability of each track within a jet to originate from the primary vertex based on its impact parameter information. This probability is multiplied track by track to determine an overall probability. The JLIP reduced probability $\text{Prob}_{\text{red}}^{\text{JLIP}}$ is the re-calculated JLIP probability with the track removed that is least probable to belong to the primary

---

[1] Particle level jets in simulated events use the generated stable particles (except muons and neutrinos) as inputs to the jet clustering algorithm instead of calorimeter clusters.
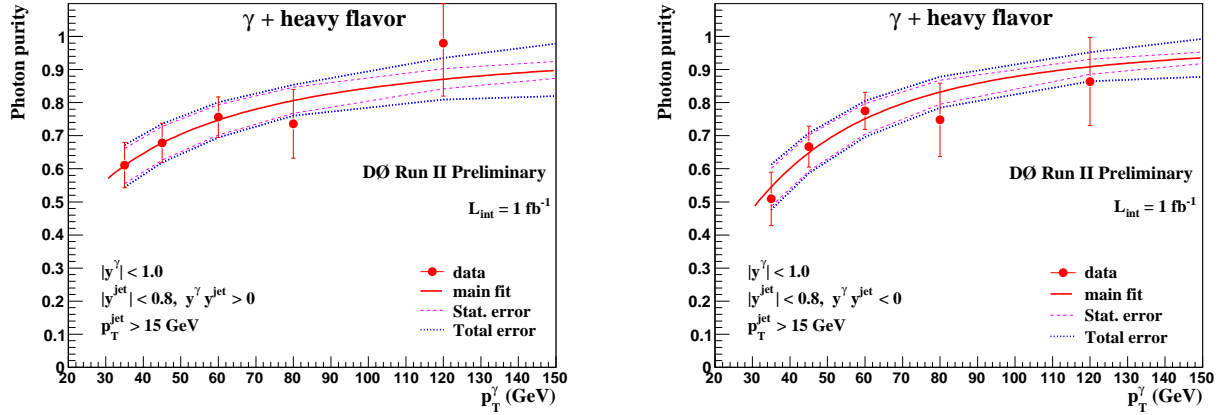
FIG. 3: The photon purity in the selected "$\gamma$ + heavy flavor jet" events as a function of $p_T^\gamma$ for the two measured configuration of photon and jet rapidities: the left plot is for region 1 and the right plot is for region 2. The result of the $(1 - \exp(a + bp_T^\gamma))$ functional fit is shown by the full lines, together with the statistical uncertainty in the default fit (dashed lines) and the total uncertainty (dotted lines).

vertex. In this way the influence of mis-measured or fake tracks on the $b$-tagging probability is reduced. We define the variable $\text{rJLIP} = -\ln(\text{Prob}_{\text{red}}^{\text{JLIP}})$, which is used later in this analysis to determine the fraction of light, $c$, and $b$ jets in the selected sample. Jets from $b$ quarks tend to have large values of rJLIP as compared to light jets whose tracks originate from the primarily vertex, leading to small values of rJLIP.

## III. ESTIMATIONS OF PHOTON PURITY AND HEAVY FLAVOR FRACTIONS.

### A. Photon Purity.

After the selection criteria have been satisfied for the event, the photon candidates, and the heavy flavor jet candidates, about 14,000 events remain. The amount of true photons as well as the fraction of $b$ and $c$ jets in the final data sample have to be determined as these events still contain non-negligible background. The photon background is mainly caused by dijet events in which one jet is misidentified as a photon signal. For the photon purity estimate $\mathcal{P} = N^\gamma/(N^\gamma + N^{\text{jet}})$, where $N^\gamma$ ($N^{\text{jet}}$) is the number of single photon (dijet) events that pass the selection criteria, the photon ANN output is used from data and is fit with Monte Carlo distributions of single photons from signal events and jets from dijet events using a maximum likelihood fit. This fit is performed in each photon $p_T$ bin for both photon-jet rapidity regions independently. These purities are $p_T$ dependent and can be parameterized using the function $\mathcal{P} = 1 - \exp(a + bp_T^\gamma)$. The resulting photon purities are shown in Fig. 3.

### B. Heavy Flavor Fractions.

In order to estimate the fractional contributions of $b$ and $c$ jets to the final data sample, we again use a maximum likelihood fit of jet flavor templates to model the overall data shape for each bin of photon $p_T$. The shape information is taken from the rJLIP variable for light, $c$ and $b$ jets and are fit to the data. The light jet template is taken directly from a light jet enriched data sample, referred to as negative tagged data, that has been corrected for $b$ and $c$ quark contributions. Both the $b$ and $c$ jet templates are taken from Monte Carlo PYTHIA [13] simulation with correction factors applied to account for differences in data and the Monte Carlo efficiencies. Once the fractional contribution of each jet flavor is determined, all three templates are weighted by their respective fractions and summed together. This distribution is normalized to the number of events in data and the two shapes are compared to test the derived fit fractions as shown in Fig. 4. The estimated fractions of $b$ and $c$ jets are shown in Fig. 5.

The $b$ and $c$ jet fractions have been cross-checked using a method that is less sensitive to the shape of the template distributions. The three unknown fractions of light, $c$, and $b$ jets can be calculated analytically by performing three measurements of the number of the selected events in data for different cuts on the rJLIP variable when the efficiencies to pass these cuts are known. The first measurement is performed without any rJLIP cut, and the second and third

measurements require rJLIP to be greater than some cut values cut1 and cut2. We calculate the efficiencies to pass these two cuts from the templates of light, $c$ and $b$ jet events used in the fit above. Multiple pairs of these cuts have been tested and the results of this *efficiency method* are all in good agreement with the template fitting technique as shown in Fig. 6.

An additional test has been done to check the $b$ and $c$ fractions found with the rJLIP variable. In this test, we preselected events after a cut of the $b$-NN output $> 0.20$ and calculated the $b$ and $c$ efficiencies from the $b$-NN output distribution using two additional cuts, 0.45 and 0.85. The efficiency method, described above, was used to determine the flavor fractions of this sample. The obtained fractions are in good agreement with those found with the use of the rJLIP variable.

We also studied the $b$-tagging efficiency and shapes of the rJLIP variable for $c, c\bar{c}$ and $b, b\bar{b}$ final states produced in the processes (1) and (2), simulated with PYTHIA. We found that both the $b$-tagging efficiency and shape of rJLIP distributions are similar between $c$ and $c\bar{c}$ events and separately between $b$ and $b\bar{b}$ events and, at the same time, are noticeably different between flavors.

## C. Cross Section Unfolding.

The measured cross section must be corrected to account for $p_T^\gamma$ smearing effects due to the finite resolution of the calorimeter. An analytical correction is performed by fitting an unfolding function to the uncorrected cross section, which is a convolution of an *ansatz* function and the measured electromagnetic energy resolution function determined from the $Z$ peak. The correction is then the ratio of the *ansatz* function to the smeared fitting function. The size of the corrections ranges from 1 to 3.5 % depending on $p_T^\gamma$ and the two kinematic regions.

## IV. CALCULATION OF CROSS SECTIONS AND COMPARISON WITH THEORY.

The cross section is calculated according to

$$\frac{\mathrm{d}^3\sigma}{\mathrm{d}p_T^\gamma \mathrm{d}y^\gamma \mathrm{d}y^{\mathrm{jet}}} = \frac{N_{\mathrm{Events}}\ \mathcal{P}_{b(c)}\ \mathcal{P}_\gamma}{\Delta y^{\mathrm{jet}}\ \Delta y^\gamma\ \Delta p_T^\gamma\ \epsilon_t\ \epsilon_s^\gamma\ \epsilon_s^{\mathrm{jet}}\ \epsilon_{pv}\ \epsilon_{b(c)}^{\mathrm{jet}}\ \epsilon_{E_T^{\mathrm{miss}}}\ L_{\mathrm{int}}\ \mathcal{A}}. \tag{3}$$

Here, $\mathcal{A}$ is the acceptance, $L_{\mathrm{int}}$ the integrated luminosity, $\mathcal{P}_{b(c)}$ the $b$ ($c$) jet fractions, and $\mathcal{P}_\gamma$ photon purity. Furthermore, $\epsilon_t$ is the trigger efficiency, $\epsilon_s^\gamma$ the photon selection efficiency, $\epsilon_s^{\mathrm{jet}}$ the jet selection efficiency, $\epsilon_{PV}$ the primary vertex cut efficiency, $\epsilon_{b(c)}^{\mathrm{jet}}$ the $b$ ($c$) tagging efficiency, and $\epsilon_{E_T^{\mathrm{miss}}}$ the $E_T^{\mathrm{miss}}$ efficiency.

The cross sections are calculated in five $p_T^\gamma$ bins and two regions of $y^\gamma y^{\mathrm{jet}}$. The resulting cross sections are shown in Fig. 7 for the $\gamma + b$ and $\gamma + c$ processes. One can see that in the range of $30 < p_T^\gamma < 150$ GeV for regions 1 and 2, for both $b$ and $c$ jets, the cross sections fall more than two orders of magnitude.

Statistical uncertainties vary from 0.2 % in the first $p_T^\gamma$ bin to 8–9 % in the last bin while systematic uncertainties vary between 15–25 % (depending on the $p_T^\gamma$ region). A break-down of the most important systematic uncertainties is shown in Fig. 8. At low $p_T^\gamma$ the main uncertainty comes from the photon purity estimation ($\sim$10.5 %) and the heavy flavor fraction estimation ($\sim$9 %). At higher $p_T^\gamma$ the total uncertainty is dominated by the heavy flavor fraction estimation ($\sim$23 % in the highest $p_T^\gamma$ bin). The heavy flavor fractions are estimated by fitting templates to the data, and the main contribution to the uncertainties on these fractions comes from the small data statistics for large $p_T^\gamma$ and from limited statistics in the $c$-jets MC template at small $p_T^\gamma$. Other significant uncertainties arise from the jet selection efficiency (between $\sim$8 % and $\sim$2 %) and the luminosity (6 %).

The theoretical predictions presented in Fig. 7 correspond to the choice of renormalization, factorization and fragmentation scales chosen as $\mu_R = \mu_F = \mu_f = p_T^\gamma$. These predictions are preliminary [32] and are based on the technique used to calculate the analytic cross sections published in Ref. [33].

The ratios of the $\gamma + b$ and $\gamma + c$ cross sections are also calculated with respect to their central theoretical predictions in regions 1 and 2 (Figs. 9 and 10). The behavior of the theoretical scale uncertainties is also shown in those figures. They are obtained by the simultaneous variation of all the three scales by a factor of two, $\mu_{R,F,f} = 0.5p_T^\gamma$, and $\mu_{R,F,f} = 2p_T^\gamma$. The theoretical predictions utilize the CTEQ6.6M PDF set with uncertainties calculated from 44 PDF sets according to the prescription in [16]. These uncertainties are shown by the shaded region in Figs. 9 and 10. The theory predictions are corrected for the effects of parton-to-hadron fragmentation and for the underlying events. The size of this correction for $b(c)$-jets varies from 7.5 % (3 %) at $30 < p_T^\gamma < 40$ GeV to 1 % at $p_T^\gamma > 90$ GeV. We find good agreement with the prediction [32] for the $\gamma + b$ cross section in the entire $p_T^\gamma$ range and for the $\gamma + c$ cross section for $p_T^\gamma < 50$ GeV. We observe a larger $\gamma + c$ cross section for $p_T^\gamma > 50$ GeV with the difference increasing with growing $p_T^\gamma$.

A possible explanation for this discrepancy is a non-negligible *intrinsic charm* (IC) content of the partons predicted by some non-perturbative models, as opposed to a common assumption of purely radiatively generated charm. This IC component is allowed to evolve from low to high energies along with other partons according to the evolution equations [10]. Another possibility is that this effect may be partially caused by existing uncertainties on the $g \to Q\bar{Q}$ fragmentation in the final state of the annihilation process that dominates at large $p_T^\gamma$. Parameterizations for two IC models have been included in the CTEQ6.6M PDF set and their ratios to the central CTEQ6.6M predictions are shown in Figs. 9 and 10. These models provide two possible arrangements of how IC could be present within partons as well as their affect on the resulting $\gamma + c$ cross section. More detailed information concerning IC models can be found in reference [10].

We also calculate the ratio $\mathcal{R}_{c/b}$ of the two cross sections and compare it to the theoretical predictions in Fig 11. Most of the systematic uncertainties cancel out in the ratio and those which remain are the ones that differ for $c$ and $b$ jets (the $c$ and $b$ fraction estimations, the $b$-tagging efficiencies and the cut on the missing transverse energy). The measured values of $\mathcal{R}_{c/b}$ agree with the predictions for $p_T^\gamma \lesssim 70$ GeV but deviate for higher values of $p_T^\gamma$. The uncertainty on the ratio is enhanced by the anti-correlation of the $c$ and $b$-jet fractions.

## V.    CONCLUSIONS.

We have measured the triple differential cross sections $\mathrm{d}^3\sigma/(\mathrm{d}p_T^\gamma \mathrm{d}y^\gamma \mathrm{d}y^{\mathrm{jet}})$ for the production of photon + $b$-jet and photon + $c$-jet for photon transverse momenta between 30 and 150 GeV, with photon rapidities of $|y^\gamma| < 1.0$, and jet rapidities of $|y^{\mathrm{jet}}| < 0.8$. This is the first $p\bar{p}$ collider measurement of the triple differential cross section for associated photon and heavy flavor production. It can also be considered as an extension and a complement to the analogous measurements of the $Z + b$ cross section performed in D0 and CDF [20].

The measured cross sections should allow coverage for the range of parton momentum fractions $x$ of $0.01 < x < 0.30$, with $0.9 \times 10^3 < (p_T^\gamma)^2 < 2 \times 10^4$ GeV$^2$, and provide information about $b$, $c$ and gluon PDFs in this region.

The measured cross sections were compared to NLO QCD predictions with the CTEQ6.6M PDF set [32]. The current results of "$\gamma + b$-jet" production show agreement within uncertainties with the theory for the entire $p_T^\gamma$ range in both rapidity regions. We also see agreement for the $\gamma + c$ cross section in both rapidity regions for $p_T^\gamma < 50$ GeV. However we see a noticeable disagreement for $\gamma + c$ production starting from $p_T^\gamma > 70$ GeV in region 1 and from $p_T^\gamma > 50$ GeV in region 2 that increases with $p_T^\gamma$.

[1] P. Aurenche, J. Lindfors, Nucl.Phys.**B168**(1980)296.
[2] E.N. Argyres, A.P. Contogouris, N. Mebarki and S. D.P. Vlassopulos, Phys. Rev. D **35**, 1584 (1987).
[3] J.F. Owens, Rev. Mod. Phys. **59**, 465 (1987).
[4] P. Aurenche, R. Baier, M. Fontannaz, J.F. Owens and M. Werlen, Phys. Rev. D **39**, 3275 (1989).
[5] E.L. Berger and J. Qiu, Phys. Rev. D **44**, 2002 (1991).
[6] W. Vogelsang and A. Vogt, Nucl. Phys. **B453**, 334 (1995).
[7] S. Frixione and W. Vogelsang, CERN-TH/99-247, hep-ph/9908387.
[8] S. Catani, M. Fontannaz, J.Ph. Guillet and E. Pilon, J. High Energy Phys. **0205**, 28 (2002).
[9] B. Bailey, E.L. Berger, L.E. Gordon, Phys. Rev. D **54**, 1896 (1996);
    E.L. Berger, L.E. Gordon, Phys. Rev. D **54**, 2279 (1996).
[10] J. Pumplin *et al.*, Phys. Rev. D **75**, 054029 (2007). See also references inside.
[11] G.C. Blazey *et al.*, arXiv:hep-ex/0005012 (2000).
[12] T. Scanlon, Ph.D. thesis, FERMILAB-THESIS-2006-43.
[13] T. Sjostrand, Comp. Phys. Comm. **82**, 74 (1995).
[14] J. Pumplin *et al.*, J. High Energy Phys. **0207**, 012 (2002).
[15] W. K. Tung, hep-ph/0409145; W. K. Tung, H. L. Lai, J. Pumplin, P. Nadolsky and C. P. Yuan, arXiv:0707.0320 [hep-ph].

[16] J. Pumplin *et al.*, J. High Energy Phys. **0207**, 12 (2002); D. Stump *et al.*, J. High Energy Phys. **0310**, 046 (2003).

[17] M. Gluck, *et al.*, Phys. Lett. B **664**, 133 (2008).

[18] D0 Collaboration, B. Abbott *et al.*, Phys. Rev. Lett. **85**, 5068 (2000). See also references inside.

[19] CDF preliminary, `http://www-cdf.fnal.gov/physics/new/qcd/QCD.html`

[20] D0 Collaboration, V. Abazov *et al.*, Phys. Rev. Lett. **94**, 161801 (2005); CDF Collaboration, A. Abulencia *et al*, Phys. Rev. D **74**, 032008 (2006).

[21] A. Alton *et al.*, Phys. Rev. D **64**, 012002 (2001).

[22] EMC Collaboration, J.J. Aubert *et al.*, Z. Phys. C **72**, 593 (1996).

[23] W. K. Tung, H. L. Lai, A. Belyaev, J. Pumplin, D. Stump and C. P. Yuan, J. High Energy Phys. **0702**, 053 (2007).

[24] D0 Collaboration, V.M. Abazov *et al.*, FERMILAB-PUB-08-056-E.

[25] S.J. Brodsky, B. Kopeliovich, I. Schmidt, J. Soffer, Phys. Rev. D **73**, 113005 (2006).

[26] H.J. He, C.P. Yuan, Phys. Rev. Lett. **83**, 28 (1999); C. Balazs,H.J. He, C.P. Yuan, Phys. Rev. D **60**, 114001 (1999).

[27] K.A.Assamagan, *et al*, hep-ph/0406152.

[28] D. Abbaneo, *et al* (The LEP/SLD heavy flavor working group), LEPHF/2001-01.

[29] D0 Collaboration, V. Abazov *et al.*, arXiv:0804.1107; Fermilab-Pub-08/081-E, Submitted to Phys. Lett. B.

[30] D0 Collaboration, V.M. Abazov *et al.*, Phys. Lett. B **653**, 378 (2007).

[31] D0 Collaboration, V.M. Abazov *et al*, Nucl. Instrum. Methods A **565**, 463 (2006).

[32] T. Stavreva, J.F. Owens, "Photon + Heavy Flavor Cross Sections (*in progress*)", 2008.

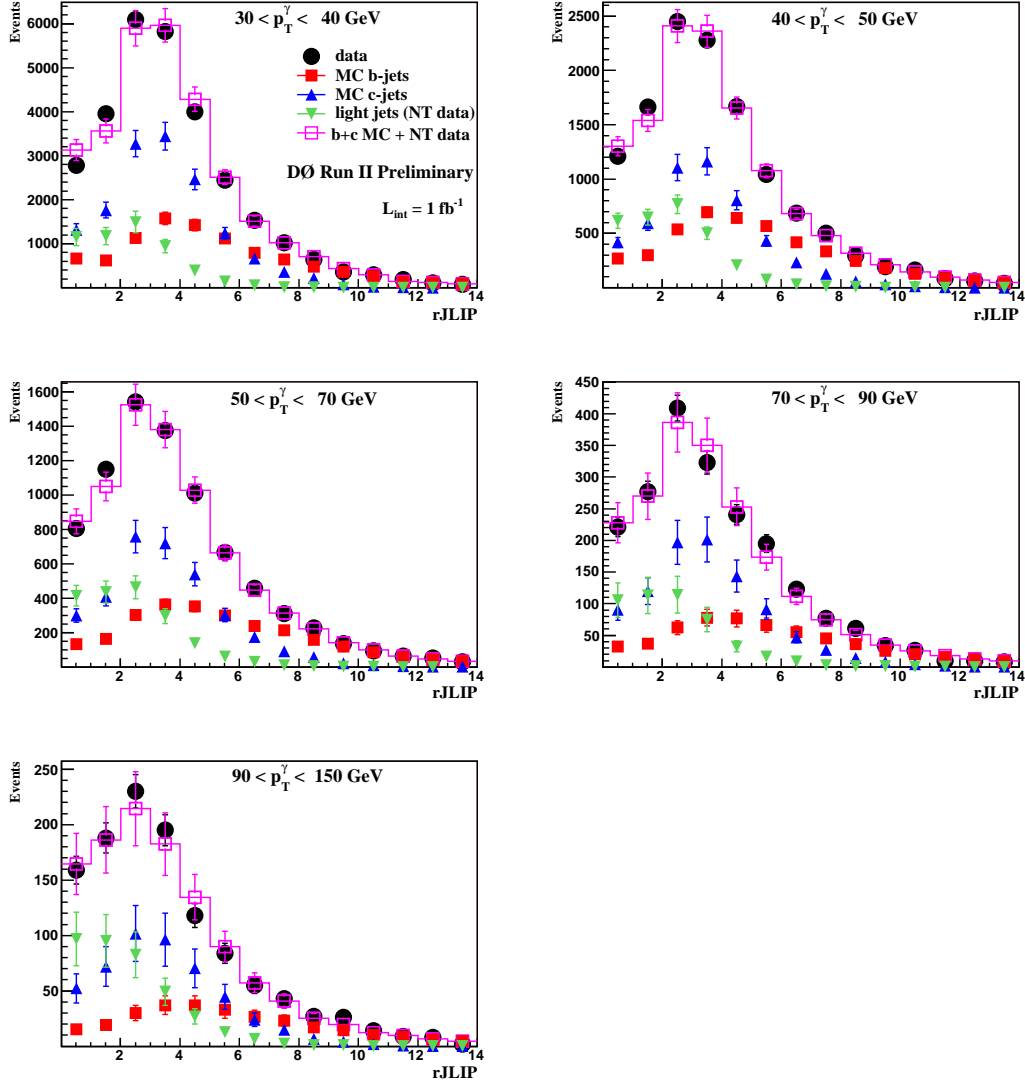[33] B.W. Harris, J.F. Owens, "The two cutoff phase space slicing method", arXiv:hep-ph/0102128v2.

FIG. 4: Distribution of the number of events in data for rJLIP after all selections, including $b$-NN output $> 0.85$, in five $p_T^\gamma$ intervals from 30 to 150 GeV. The fitted distributions (to the data) of the MC $b$-, $c$-jets and light jets (negatively tagged (NT) data) are also shown. They are weighted by their fractions found from the fit. The error bars show the total uncertainty caused by statistics and uncertainty from the flavor fraction fitting.
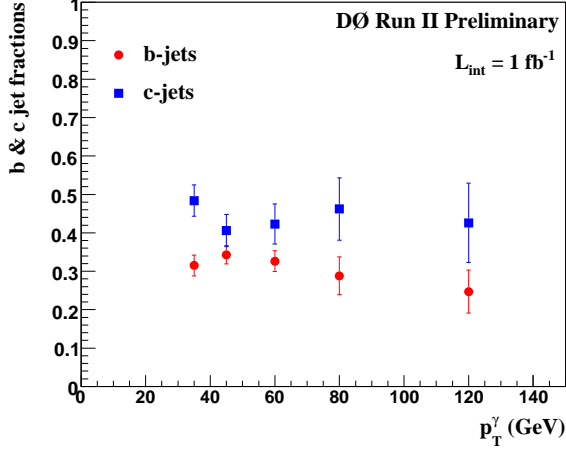
FIG. 5: Fractions of *c*- and *b*-jets vs. $p_T^\gamma$ in the "γ+jet" sample after all selection cuts.
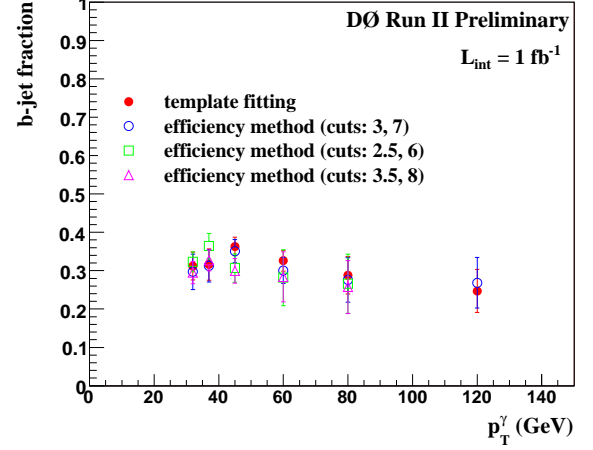
FIG. 6: The *b*-jet fraction found by the fitting method compared to those found by the efficiency method using three different values for cut1 and cut2.
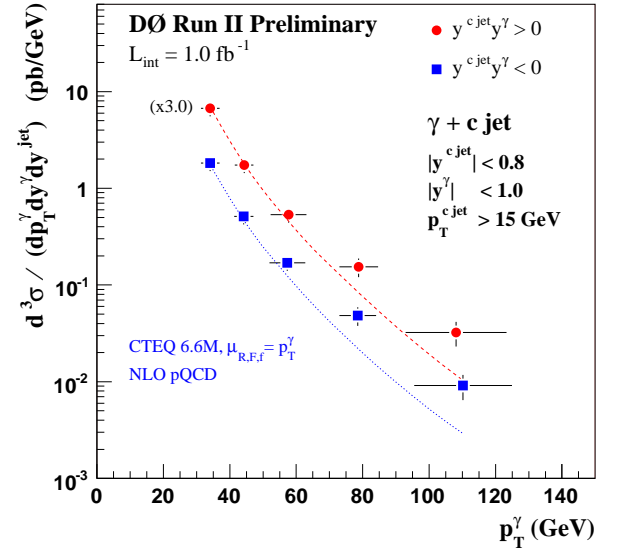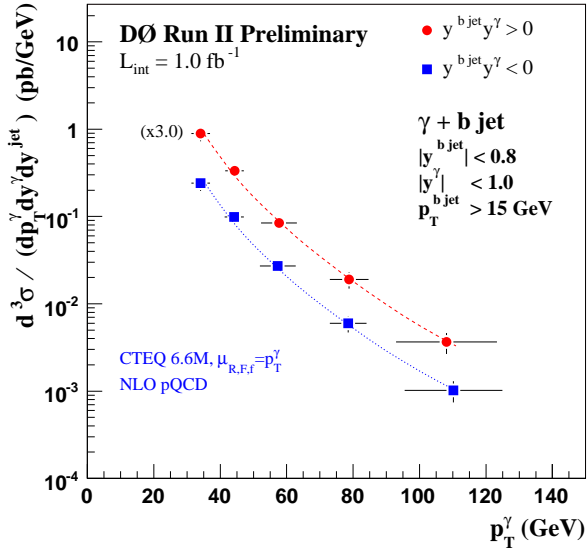


FIG. 7: The "γ + *b*-jet" (left) and "γ + *c*-jet" (right) cross sections as a function of $p_T^\gamma$ in regions 1 (multiplied by a factor of three) and 2. The uncertainties on the points in data are the full uncertainties. The NLO theoretical predictions are calculated using CTEQ6.6M and are shown by the dotted lines.
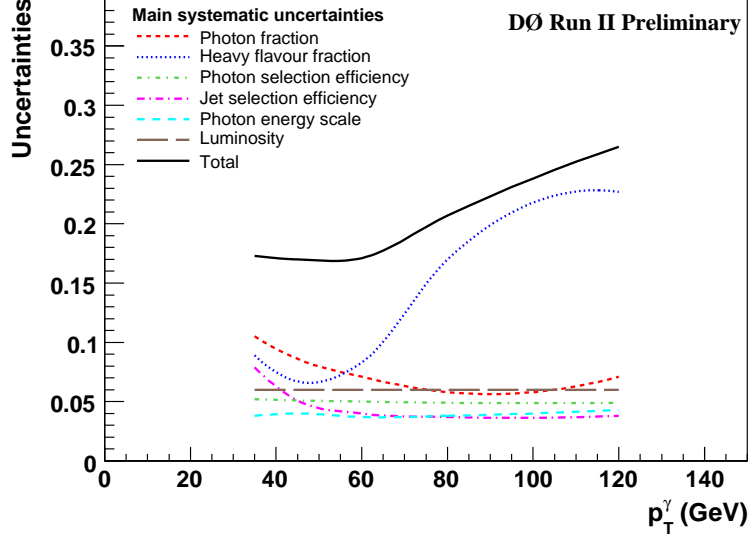
FIG. 8: The main systematic uncertainties for the triple differential cross section measured in region 1 for $\gamma + b$-jet production. Uncertainties for region 2 differ by $\leq 2\%$. The variation for $\gamma + c$-jet production is of the same size.
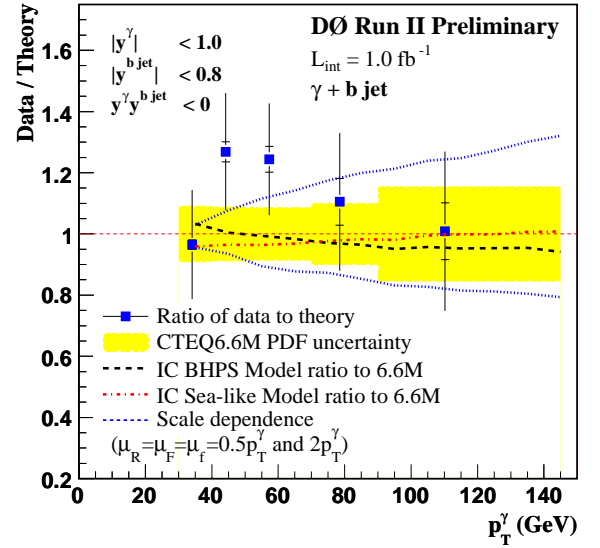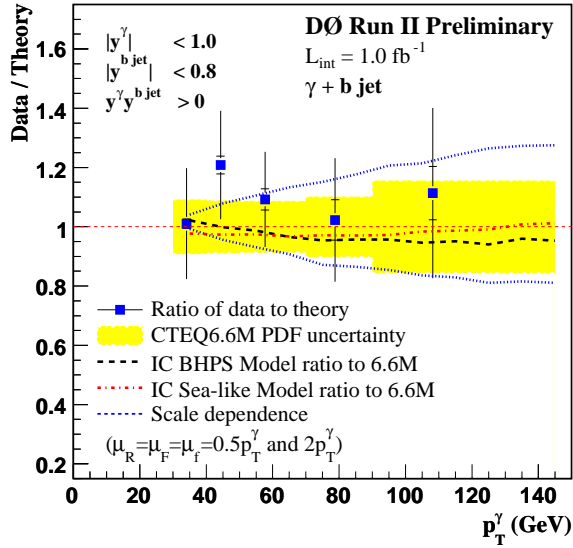


FIG. 9: The "$\gamma + b$-jet" cross section ratio of data to theory as a function of $p_T^\gamma$ in region 1 (left) and region 2 (right). This includes the theoretical scale uncertainties as well as the CTEQ6.6M PDF uncertainties. The uncertainties on the points in data include both statistical (inner line) and the full uncertainties (the entire line). The ratio of the central CTEQ6.6M prediction to two *intrinsic charm* models is also shown.
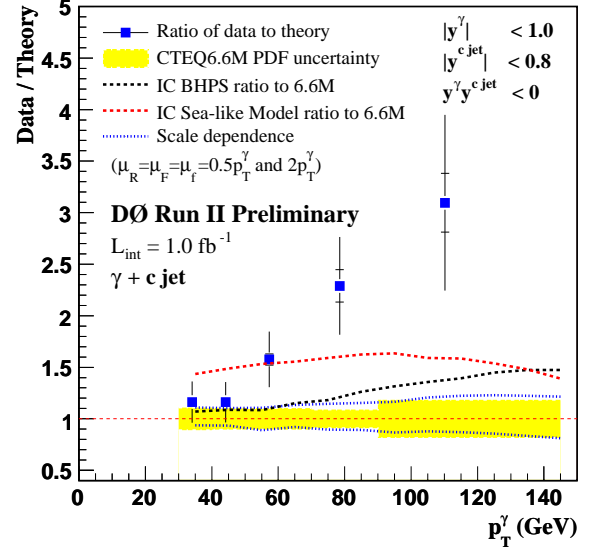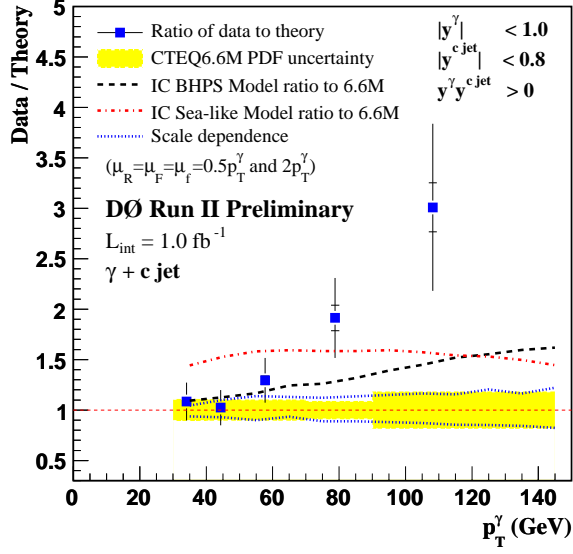
FIG. 10: Similar plots as for Fig. 9 but for the "$\gamma + c$-jet" cross section.



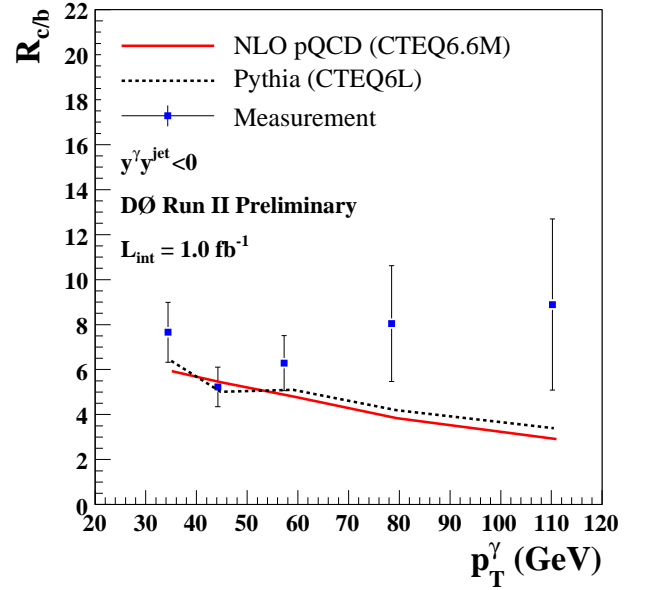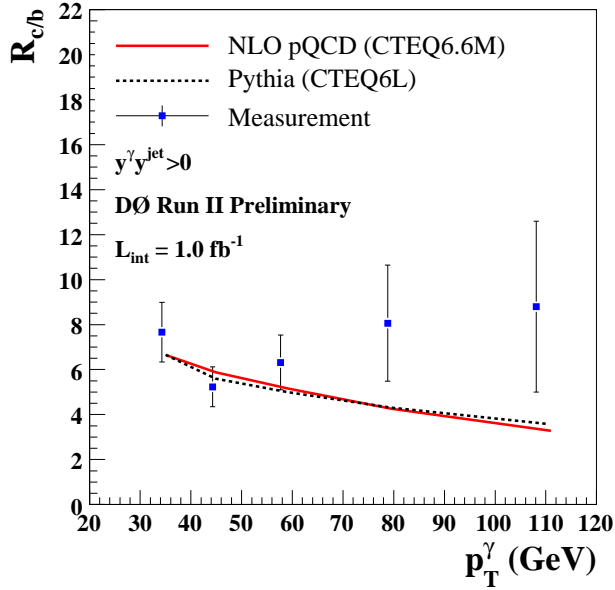FIG. 11: Ratio of the triple differential cross sections for "$\gamma + c$-jet" and "$\gamma + b$-jet" production for region 1 (left) and region 2 (right).